

# Effect of base material temper condition on precipitate evolution and mechanical properties of 2195 Al—Li alloy friction stir welding joints

Peng Chen<sup>a,b,c,\*</sup>, Wenhao Chen<sup>a</sup>, Jiaxin Chen<sup>c</sup>, Zhiyu Chen<sup>a</sup>, Ruixiang Yin<sup>a</sup>, Yang Tang<sup>d</sup>, Ge Liu<sup>e</sup>, Bensheng Huang<sup>a,b,\*</sup>, Zhiqing Zhang<sup>c,\*\*</sup>

<sup>a</sup> School of New Energy and Materials, Southwest Petroleum University, Chengdu 610500, China

<sup>b</sup> Sichuan Provincial Engineering Research Center of Advanced Materials Manufacturing Technology for Shale Gas High-Efficient Exploitation, Southwest Petroleum University, Chengdu 610500, China

<sup>c</sup> College of Materials Science and Engineering, Chongqing University, Chongqing 400045, China

<sup>d</sup> School of Mechatronic Engineering, Southwest Petroleum University, Chengdu 610500, China

<sup>e</sup> School of Robot Engineering, Yangtze Normal University, Chongqing 408100, China

## ARTICLE INFO

### Keywords:

2195 Al—Li alloy  
Friction stir welding  
Temper conditions  
Precipitates  
Mechanical properties

## ABSTRACT

In this study, 2195 Al—Li alloy plates with different temper conditions (O, T4 and T8) were subjected to friction stir welding (FSW). Precipitate evolution of the three FSW joints (2195-O/T4/T8 joint) was investigated by transmission electron microscopy (TEM). Mechanical properties of these joints were analyzed using micro-hardness and tensile test. Efforts were made to explore the correlation between precipitates, mechanical properties and fracture behavior of the joints. It can be found that the precipitates from the base material are unevenly dissolved in the nugget zone (NZ) of the 2195-O joint, while the original precipitates mostly disappear in NZ of the 2195-T8 joint, and change a little in the NZ of the 2195-T4 joint. In the thermal-mechanically affected zone (TMAZ) of the 2195-O and 2195-T4 joint, precipitates are almost unchanged, while in the TMAZ of the 2195-T8 joint, most of the precipitates are dissolved and the residual is significantly coarsened. Little change of precipitates occurs in the heat affected zone (HAZ) of the 2195-O joint. T<sub>1</sub> newly forms in the HAZ of the 2195-T4 joint (T4-HAZ), while this precipitate is mainly dissolved and coarsened in the HAZ of the 2195-T8 joint (T8-HAZ). Moreover, both grain boundary phases (GBPs) and precipitate-free zone (PFZ) are generated in the T4-HAZ and T8-HAZ. Hardness profile is represented as a “n” shape in the 2195-O joint due to significant harden of the NZ, a “wave line” shape in the 2195-T4 joint attributed to the slight change of precipitation degree, and a “w” shape in the 2195-T8 joint mainly owing to the dissolution and coarsening of T<sub>1</sub>. The three joints are all broken in their weak regions during tensile test and have a similar fracture behavior, indicating that the crack initiation and development are related to the GBPs and PFZ.

## 1. Introduction

Aluminum-lithium alloy has become one of the primary structural materials in the aerospace industry with the advantage of successfully combining of low density and high strength, since the addition of 1% Li in Al based material can decrease the density by 3% while increasing elastic modulus by 6% [1,2]. As a typical representative of the third-generation Al—Li alloys, 2195 Al—Li alloy has been widely used in the production of rocket fuel storage tank and aircraft skin due to its more excellent specific strength and cryogenic performance [3].

Recently, this alloy has also been successfully used in manufacturing fuselage as well as, upper and lower wings on C919 [4].

In the aerospace industry, the manufacturing of supersize Al—Li alloy overall structure has become a key technological breakthrough, and efficient joining process is a challenge for the high-strength Al—Li alloy [2]. The conventional fusion welding processes, such as tungsten inert gas, metal inter-gas, laser beam welding, are almost unable to obtain a high integrity joint, resulting from the critical problems of welding distortion, hot crack and porosity, especially the evaporation loss for Li [5]. As an advanced solid phase connection technology,

\* Correspondence to: Peng Chen, Bensheng Huang, School of New Energy and Materials, Southwest Petroleum University, Chengdu 610500, China.

\*\* Correspondence to: Zhiqing Zhang, College of Materials Science and Engineering, Chongqing University, Chongqing 400045, China.

E-mail addresses: [xd\\_chenpeng@163.com](mailto:xd_chenpeng@163.com) (P. Chen), [hbslxp@163.com](mailto:hbslxp@163.com) (B. Huang), [zqzhang@cqu.edu.cn](mailto:zqzhang@cqu.edu.cn) (Z. Zhang).

friction stir welding (FSW) usually generates at 0.6–0.9 Tm (Tm is melting temperature in Kelvin), commendably avoiding most of drawbacks introduced by fusion welding [6]. Therefore, this technology has been considered as an ideal welding method for Al–Li alloy, and numerous studies on Al–Li alloys friction stir welding are reported.

Most of studies have discussed the effect of welding parameters (generally about rotation speeds and welding speeds) on microstructure and mechanical properties of Al–Li alloy FSW joints [2]. Therefore, welding process windows for Al–Li alloys in different chemical component and plate thickness have been established, and mechanical properties of the joints are obviously improved [5]. Material flow behavior, thermal mechanical history and microstructure evolution rule during FSW of Al–Li alloys have also been studied in detail [5,7]. To further increase the mechanical properties of Al–Li alloy FSW joints, some novel FSW technologies, such as dual-rotation friction stir welding (DR-FSW) [8], stationary shoulder friction stir welding (SS-FSW) [9] and ultrasound assisted friction stir welding (UA-FSW) [10], are explored. As a result, tensile strength of Al–Li alloy FSW joint has been significantly enhanced, indicating the ultimate tensile strength (UTS) achieving about 495 MPa [11]. However, as compared with the strength of base material (more than 600 MPa), the obtained maximum joint strength is still lower. Thus, some researchers have conducted post welding heat treatment (PWHT) on Al–Li alloy FSW joints, controlling the precipitates and mainly promoting the generation of high density of nanoprecipitates [12]. As a result, the joint strength is dramatically raised and even equal to the strength of the base material in artificial aging (T6) temper condition [13].

Al–Li alloy belongs to precipitation-hardened aluminum alloys, whose mechanical properties mainly depend on the type, size and distribution of precipitates. 2195 Al–Li alloy has complex precipitate systems, including Guinier-Preston Zones (GPZs),  $\theta'$  ( $\text{Al}_2\text{Cu}$ ),  $\delta'$  ( $\text{Al}_3\text{Li}$ ),  $\beta'$  ( $\text{Al}_3\text{Zr}$ ),  $S'$  ( $\text{Al}_2\text{CuMg}$ ),  $T_1$  ( $\text{Al}_2\text{CuLi}$ ),  $T_B$  ( $\text{Al}_{7.5}\text{Cu}_4\text{Li}$ ) and  $T_2$  ( $\text{Al}_6\text{CuLi}$ ), and possibly  $\sigma$  ( $\text{Al}_5\text{Cu}_6\text{Mg}$ ) and  $T$  ( $\text{Al}_{20}\text{Cu}_2\text{Mn}_3$ ) as well [14].  $T_1$  is the predominant strengthening precipitate in 2195 Al–Li alloy, greatly deciding its mechanical properties [15]. Therefore, researchers pay close attention to the  $T_1$  evolution when it comes to friction stir welding of 2xxx Al–Li alloys [16–18].

It has been demonstrated that  $T_1$  has a hexagonal structure with lattice parameters  $a = 0.4965$  nm and  $c = 0.9345$  nm [15]. The plate-like  $T_1$  precipitates possess four variants developing along the (111) habit plane of the Al matrix, indicating that the orientation relationships of the precipitates with the matrix can be expressed as:  $(0001)_{T_1} // \{111\}_{\text{Al}}$  and  $\langle 10\bar{1}0 \rangle_{T_1} // \langle \bar{1}10 \rangle_{\text{Al}}$  [16]. Furthermore, under transmission electron microscope (TEM) observation along  $[110]_{\text{Al}}$  zone axis, the  $T_1$  precipitates represent different morphological features [19]. This means that two edge-on configurations, such as  $T_1^{(1\#)}$  and  $T_1^{(3\#)}$  are observed as needle-like shapes, and their orientation relationships with the Al matrix are respectively described as  $(0001)_{T_1} // (1\bar{1}1)_{\text{Al}}$ ,  $[10\bar{1}0]_{T_1} // [110]_{\text{Al}}$ , and  $(0001)_{T_1} // (1\bar{1}\bar{1})_{\text{Al}}$ ,  $[10\bar{1}0]_{T_1} // [110]_{\text{Al}}$ , as shown in Fig. 1. The other two variants of  $T_1$  (i.e.,  $T_1^{(2\#)}$  and  $T_1^{(4\#)}$ ) have orientation relationships with the matrix as follows:  $(0001)_{T_1} // (111)_{\text{Al}}$ ,  $[10\bar{1}0]_{T_1} // [\bar{1}10]_{\text{Al}}$ , and  $(0001)_{T_1} // (11\bar{1})_{\text{Al}}$ ,  $[10\bar{1}0]_{T_1} // [\bar{1}10]_{\text{Al}}$ , which are seldom viewed. However, when the size of the two variants coarsen enough, they can also be observed with elliptical-like shapes along  $[110]_{\text{Al}}$  zone axis, as shown in Fig. 1. The  $T_1$  precipitates with needle-like shapes are often observed in Al–Li alloy FSW joints, while the phases with elliptical-like shapes are rarely reported [20,21]. Shen et al. finds that numerous  $T_1$  precipitates developed in the BM dissolve in nugget zone (NZ) and thermally-mechanically affected zone (TMAZ), and coarsen in heat affected zone (HAZ), resulting in the loss of joint strength [22]. However, Chen et al. reports that  $T_1$  mostly dissolves in the TMAZ I, but coarsens in TMAZ II [23]. Besides, the researchers have also demonstrated that this precipitate completely dissolves in the NZ, and can re-forms at the top of the NZ under high rotation speeds [18]. In summary, the dissolution, coarsening and precipitation of  $T_1$  can occur

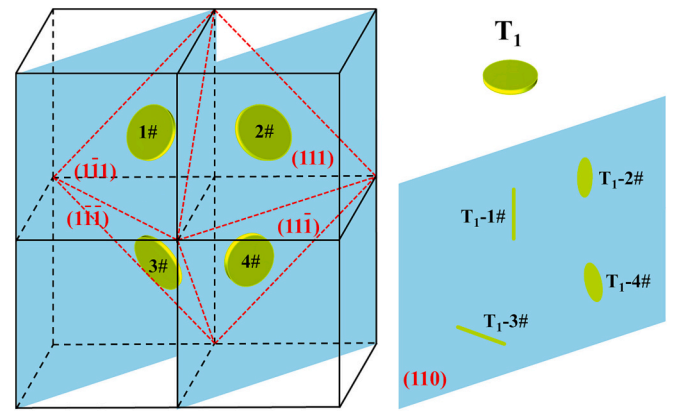


Fig. 1. Along the  $[110]_{\text{Al}}$  zone axis, four variants of  $T_1$  in the Al matrix: the  $T_1^{(1\#)}$  and  $T_1^{(3\#)}$  precipitates appear with edge-on configuration along  $(1\bar{1}1)_{\text{Al}}$  and  $(1\bar{1}\bar{1})_{\text{Al}}$ , respectively. The other variants of  $T_1^{(2\#)}$  and  $T_1^{(4\#)}$  precipitates are without edge-on configuration.

during the friction stir welding of Al–Li alloys, and softening of the joints is mostly attributed to the dissolution and coarsening of this precipitate.

$\theta'$  is another important strengthening precipitate and has a plate-like shape, which dramatically influences mechanical properties of 2195 Al–Li alloy [14]. The evolution of  $\theta'$  is similar to  $T_1$  during the friction stir welding of Al–Li alloys [16,24,25]. In addition, the precipitation behaviors of  $\delta'$  and  $\beta'$  are also discussed in Al–Li alloy FSW joints [24,26]. The  $\delta'$  with a spherical shape dissolves in the matrix due to high temperature at first, and ordinarily re-precipitate along with  $\beta'$  at the cooling process after welding [26]. The  $\beta'$  mainly involves coarsening and precipitation behavior during the FSW due to its high stability [27]. It is notable that  $\delta'$  and  $\beta'$  precipitates have the same morphology and crystal structure, and very close lattice parameters. Hence, the both are usually recognized as  $\delta'/\beta'$  in Al–Li alloy FSW joints [24,28]. The  $T_B$ ,  $\sigma$  and  $S'$  are also detected in Al–Li alloy FSW joints, resulting from the effect of the thermal history [5,20,28].

It is worth noting that, in the studies of Al–Li alloy friction stir welding, most base materials (BM) are used with a peak artificial aging (T8) temper condition [29–31]. Thus, the precipitation behaviors and mechanical properties of Al–Li alloy FSW joints based on other temper conditions of Al–Li are not exactly clear. Mariana et al. studied the microstructure of AA2098-T351 Al–Li alloy joint, and mainly focused on the precipitation behaviors of different regions of the joint, but did not report about the joint properties [32]. Malard et al. found that very little precipitation taken place during the friction stir welding of 2050-T34 Al–Li alloy, leading to almost unchanged hardness distribution of the joint [25]. Wesley et al. reported the fracture behaviors of 2195-O Al–Li alloy FSW joint based grain orientation analysis, while lack of discussion about precipitate evolution [33]. Chen et al. studied precipitate evolution in 2195-O Al–Li alloy FSW joint, indicating that the dissolution of the coarse equilibrium phases enhanced the NZ, and the difference of the dissolution degree led to heterogenous hardness distribution within the NZ [27].

Consequently, different precipitate features can be detected in the Al–Li alloy FSW joints when the base materials are in variant temper conditions, which will significantly affect mechanical properties of the joints. However, corresponding studies about the joints, which are manufactured from the BM with different temper conditions, have not been reported in public. To provide a deeper insight into this issue, 2195 Al–Li alloy plates received in three different temper conditions, namely, peak artificial aging (T8), natural aging (T4) and complete annealing (O), are subjected to friction stir welding. The relationships of the precipitates, mechanical properties and fracture behaviors in the different joints are discussed in detail.

## 2. Material and experimental work

In this study, 7.5 mm thick 2195 Al–Li alloy plates obtained with three different temper conditions (T8, T4, O) were subjected to friction stir butt welding with a rotation speed of 700 rpm and a welding speed of 50 mm/min. The base materials in O, T4 and T8 temper conditions are named 2195-O, 2195-T4 and 2195-T8, respectively, and corresponding FSW joints are expressed as 2195-O, 2195-T4 and 2195-T8 joints. Chemical compositions of the as-received 2195 Al–Li alloy were listed in Table 1. Welding process was carried out with a shoulder plunge depth of 0.1 mm and a tool tilt angle of 2.5°. FSW tool is made of high-speed steel and consists of a concave shoulder with 18 mm in diameter and a threaded taper cylindrical pin with 6.9 mm in length.

Precipitate characterization was conducted by TEM (Talos F200S) and DSC (NETZSCH DSC 404F3). Scanning transmission electron microscopy (STEM), high resolution transmission electron microscopy (HRTEM), selected area electron diffraction (SAED) and fast Fourier transform (FFT) analysis technologies are mainly used to explore precipitate features in the different regions of the joints. TEM samples were prepared by two methods: one was twin-jet electro-polishing with a solution of 70% CH<sub>3</sub>OH and 30% HNO<sub>3</sub> at 15 V and –30 °C, and the other was focused ion beam (FIB) technology by Zeiss Auriga FIB-SEM. The samples (25–30 mg) for DSC measurement were cut from the base material with different temper conditions. The DSC analysis was carried in a crucible made of Al at the heating rate of 10 °C/min. The Micro-hardness profiles were measured on the transverse cross-section of joints by MH-5 L micro-hardness testers. The measurement was carried out in the middle thickness of the joints with an interval of 0.5 mm under a load of 500 g for 10 s. Tensile test specimens were prepared as per ASTM: E8–M11 guidelines, and three samples were tested for each condition. Room-temperature tensile tests were carried out using AG-X testing machines (maximum load of 50 kN, accuracy of ±0.5%) with a displacement state of 1 mm/min. Fracture morphologies of the base materials and joints were observed by the SEM.

## 3. Results

### 3.1. Hardness profiles

Hardness profiles of the three kinds of 2195 Al–Li FSW joints are shown in Fig. 2. A typical “w” shaped hardness profile for 2195-T8 joint is observed, while the hardness profile for the 2195-T4 joint and 2195-O joint is exhibited a “wavy line” and “n” shape, respectively. The 2195-T8 joint develops significant softening regions, comprising NZ, TMAZ and HAZ, while softening is not remarkable in the 2195-T4 joint. It is noticeable that the 2195-O joint is obviously hardened in the NZ.

The hardness of the BM in O, T4 and T8 temper condition is 58 HV<sub>0.5</sub>, 132 HV<sub>0.5</sub> and 190 HV<sub>0.5</sub>, respectively. Average hardness of the NZ is higher in the 2195-T4 joint (132.2) than the 2195-O joint (108.4 HV<sub>0.5</sub>) and 2195-T8 (124.8 HV<sub>0.5</sub>) joint. Moreover, in the 2195-T8 joint, hardness of the NZ is significantly decreased, while in the 2195-T4 joint, hardness of the NZ is almost changed. Besides, in the 2195-O joint, hardness of the NZ is distinctly higher than its BM. As for the NZ inners, hardness fluctuates in a narrow range in the 2195-T4 joint and 2195-T8 joint, but significantly reduces from the advance side (AS–NZ, about 133 HV<sub>0.5</sub>) to retreating side (RS–NZ, about 65 HV<sub>0.5</sub>) in the 2195-O joint.

As compared with the BM, hardness of the TMAZ is increased (5–20 HV<sub>0.5</sub>) in the 2195-O joint, dramatically decreased in the 2195-T8 joint (about 60 HV<sub>0.5</sub>), and changed a little in the 2195-T4 joint. It is worth noting that the size of the TMAZ in different joints is not consistent. The

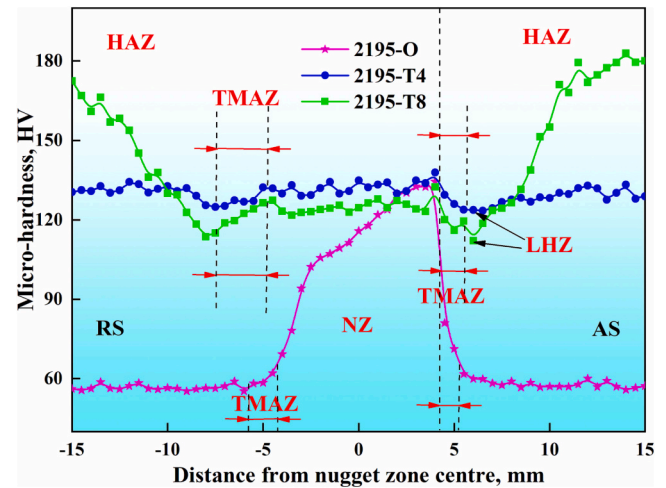


Fig. 2. Hardness profiles of 2195 Al–Li alloys FSW joints.

TMAZ of the 2195-O joint appears smaller compared to the other two joints, while the TMAZ of 2195-T8 and 2195-T4 joints are approximately equal in size. Furthermore, hardness of the HAZ is almost unchanged in the 2195-O joint and 2195-T4 joint, but obviously decreased in the 2195-T8 joint. The lowest hardness zone (LHZ) is generated at the transition zone between the HAZ and TMAZ in the 2195-T4 joint and 2195-T8 joint, while the LHZ is not obvious in the 2195-O joints.

### 3.2. Precipitates characterization

2195 Al–Li alloy is a kind of typical precipitation strengthening Al alloy, indicating that mechanical properties of this alloy and corresponding FSW joint are mainly determined by precipitates [16,24]. In order to further understand the hardness distribution of the three FSW joints which are manufactured with different temper conditions of base material, precipitates in the typical regions of the joints are analyzed in detail. The macro-morphology in the cross-section of the three joints are exhibited in Fig. 3. In addition, the TEM observation regions are labeled ‘1’ to ‘4’ in the NZ, AS-TMAZ, LHZ and AS-HAZ, respectively.

#### 3.2.1. Precipitates in the BM

Precipitates of the three temper conditions of the BM (O-BM, T4-BM and T8-BM) are analyzed by DSC and TEM. The DSC curves of the BM are plotted as the function of heat flow and temperature in Fig. 4, and the precipitate observation by TEM are presented in Fig. 5.

##### (1) DSC analysis.

According to the conventional precipitation sequence of Al–Cu–Li alloys, the first endothermic peak (labeled as peak ‘a’) at the temperature ranging from 110 °C to 160 °C in the DSC curves corresponds dissolution of GP zones [14,32]. The second endothermic peak at the temperature between 170 °C and 250 °C (defined as peak ‘b’) is about dissolution of δ' [14,21]. The exothermic peak (namely peak ‘c’) at the temperature ranging from 250 °C to 330 °C indicates precipitation of T<sub>1</sub> [21].

As shown in Fig. 4, only the dissolution of GP zones is found in the curves of O-BM, indicating the presence of these solute clusters before heating. In the DSC curves of the T4-BM, dissolution of GP zones and δ' is obviously detected, which is indicative of the development of these precipitates with relatively bigger contents. Furthermore, the T<sub>1</sub> precipitation peak with a large area is observed in the T4-BM, indicating that a large number of solutes reserves in the matrix before heating and lots of T<sub>1</sub> precipitates are generated during the heating. As for the T8-BM, a smaller precipitation peak (formation of T<sub>1</sub>) is detected in the

Table 1

Chemical compositions of the 2195-T8 Al–Li alloys (wt. %).

Cu	Li	Mg	Ag	Zr	Fe	Al
4.00	1.00	0.44	0.40	0.11	0.05	Bal.



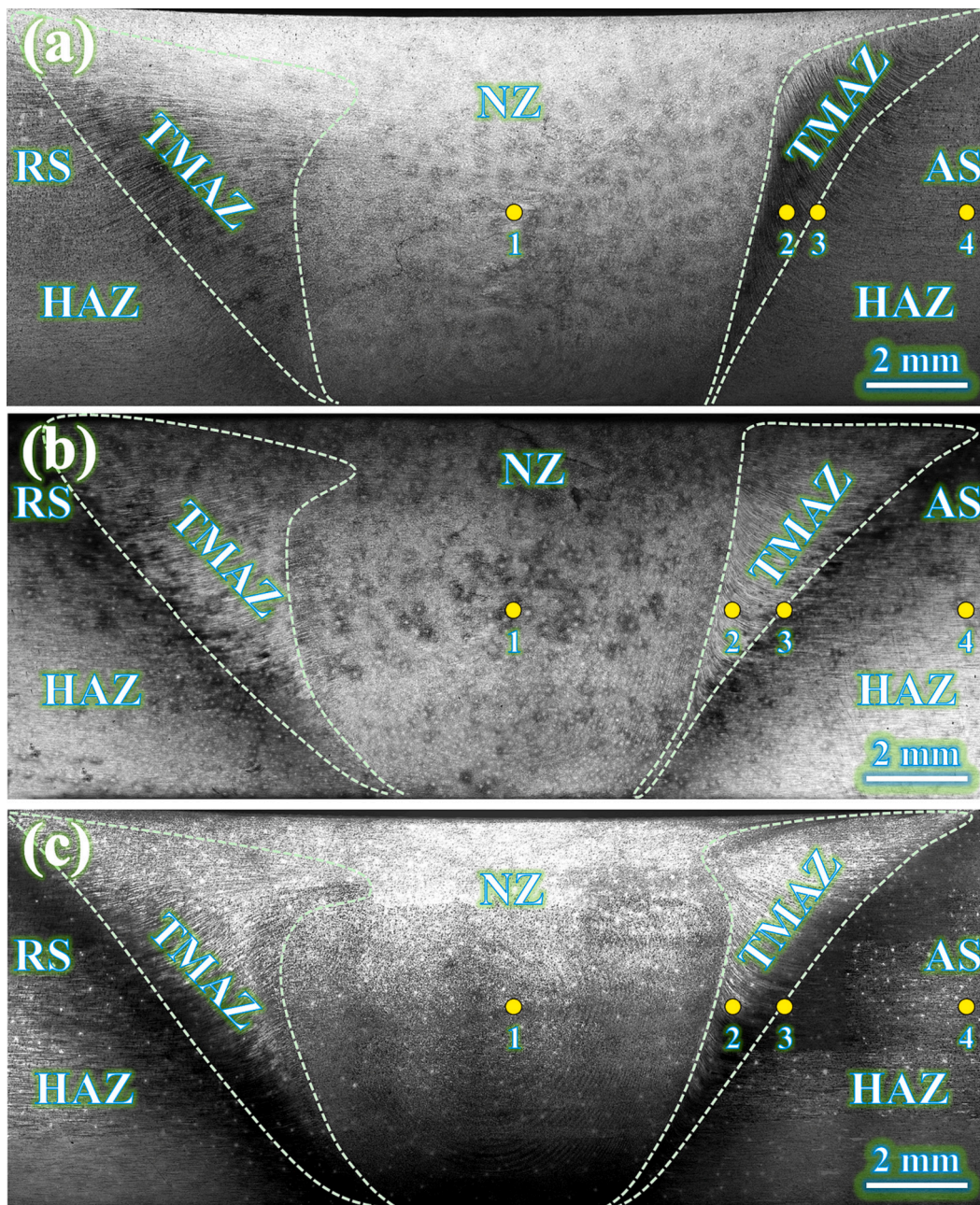


Fig. 3. The macro-morphology in the cross-section of (a) 2195-O joint; (b) 2195-T4 joint; (c, d) 2195-T8 joint.

DSC curves, and the peak temperature is obviously higher in the T8-BM (about 299.5 °C) than the T4-BM (about 265.8 °C), which means that lower precipitation kinetics generates in the T8-BM.

## (2) TEM characterization.

According to the Fig. 5a and d, coarse phases (about 0.8  $\mu\text{m}$ ) and fine spherical precipitates are observed in the O-BM. The coarse phases belong to equilibrium phases, mainly consisting of  $\text{Al}_{7.5}\text{Cu}_4\text{Li}$  ( $T_B$ ),  $\text{Al}_7\text{Cu}_2\text{Fe}$ ,  $\text{Al}_6\text{CuMg}_4$  ( $T$ ) and  $\text{Al}_2\text{Cu}$  ( $\theta$ ), which are identified in our previous studies [27]. The fine precipitates are  $\delta'$  (about 10 nm) and  $\beta'$  (about 20–40 nm), both of which have same morphology and crystal structure, and very similar lattice parameters [28]. Thus, the two precipitates are always referred to as  $\delta'/\beta'$  in Al–Li alloys [18,23,24].

In the T4-BM, many  $\delta'/\beta'$  can be identified by their morphology exhibited in Fig. 5b and e. GP zones with mono-layer Cu atoms are also

detected using HRTEM and FFT as shown in Fig. 5g–i. The observation results by TEM are in accordance with the detections by DSC (Fig. 4).

In the T8-BM, high density of  $T_1$  (about 50–120 nm in length and 2–5 nm in thickness) is viewed with a needle-like shape, indicating that the precipitate mainly belongs to the 1# and 3# variants of  $T_1$  ( $T_1^{(1/3\#)}$ ), as shown in Fig. 5c and f. Moreover, a few  $\delta'/\beta'$  and  $\theta'$  are also found with a little size.

### 3.2.2. Precipitates in the NZ

Precipitates in the NZ of 2195-O, 2195-T4 and 2195-T8 joint are exhibited in Fig. 6. According to the hardness distribution of the NZ in 2195-O joint (O-NZ in Fig. 2), precipitates in the AS-NZ and RS-NZ of the joints are analyzed, respectively, as shown in Fig. 6a and d. It can be found that the original coarse equilibrium phases completely disappear in the AS-NZ with many fine  $\delta'/\beta'$  (5–30 nm) generating (Fig. 6a). However, these coarse phases remain in the RS-NZ, showing evidently



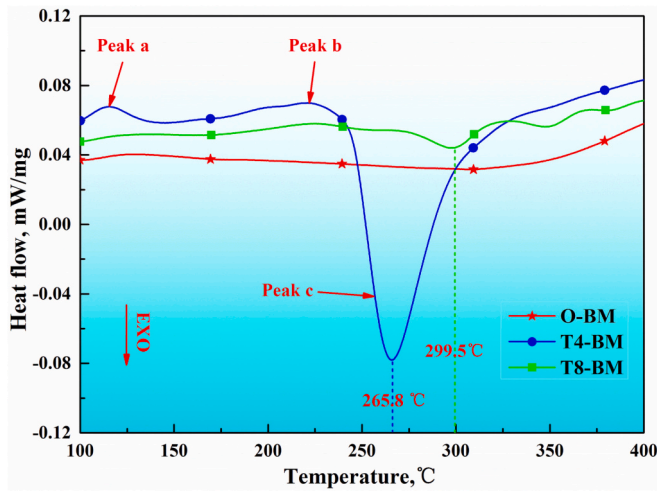


Fig. 4. DSC thermograms of the different base material.

decrease in content and size of the phase and having a length about 0.2–0.4  $\mu\text{m}$  (Fig. 6d).

Precipitates in the NZ of 2195-T4 joint (T4-NZ, Fig. 6) are similar to those in the T4-BM (Fig. 5b) indicating the presence of many  $\delta'/\beta'$ , as shown in Fig. 6b. While, the difference is about the generation of a few needle-like precipitates in the T4-NZ, which are proved to be  $T_1$  by morphology, orientation and lattice structure analysis under STEM and HRTEM, as shown in Fig. 6e. As indicated by Figs. 6c and f,  $T_1$  nearly entirely dissolves within the T8-NZ, enhancing the formation of high-density  $\delta'/\beta'$  and rod-shaped precipitates. According to literatures, these rod-shaped precipitates might be several other equilibrium phases ( $T_2$  or  $T_B$ ) [16,18,28].

### 3.2.3. Precipitates in the TMAZ

Precipitates of the TMAZ of 2195-O, 2195-T4 and 2195-T8 joint are exhibited in Fig. 7. According to the Fig. 7a and d, the presence of large coarse equilibrium phases in the TMAZ of 2195-O joint (O-TMAZ) is similar to the O-BM. In addition, high density of dislocations pinned by  $\delta'/\beta'$  precipitates is found in this region.

Fig. 7b and e show precipitates in the TMAZ of 2195-T4 joint (T4-

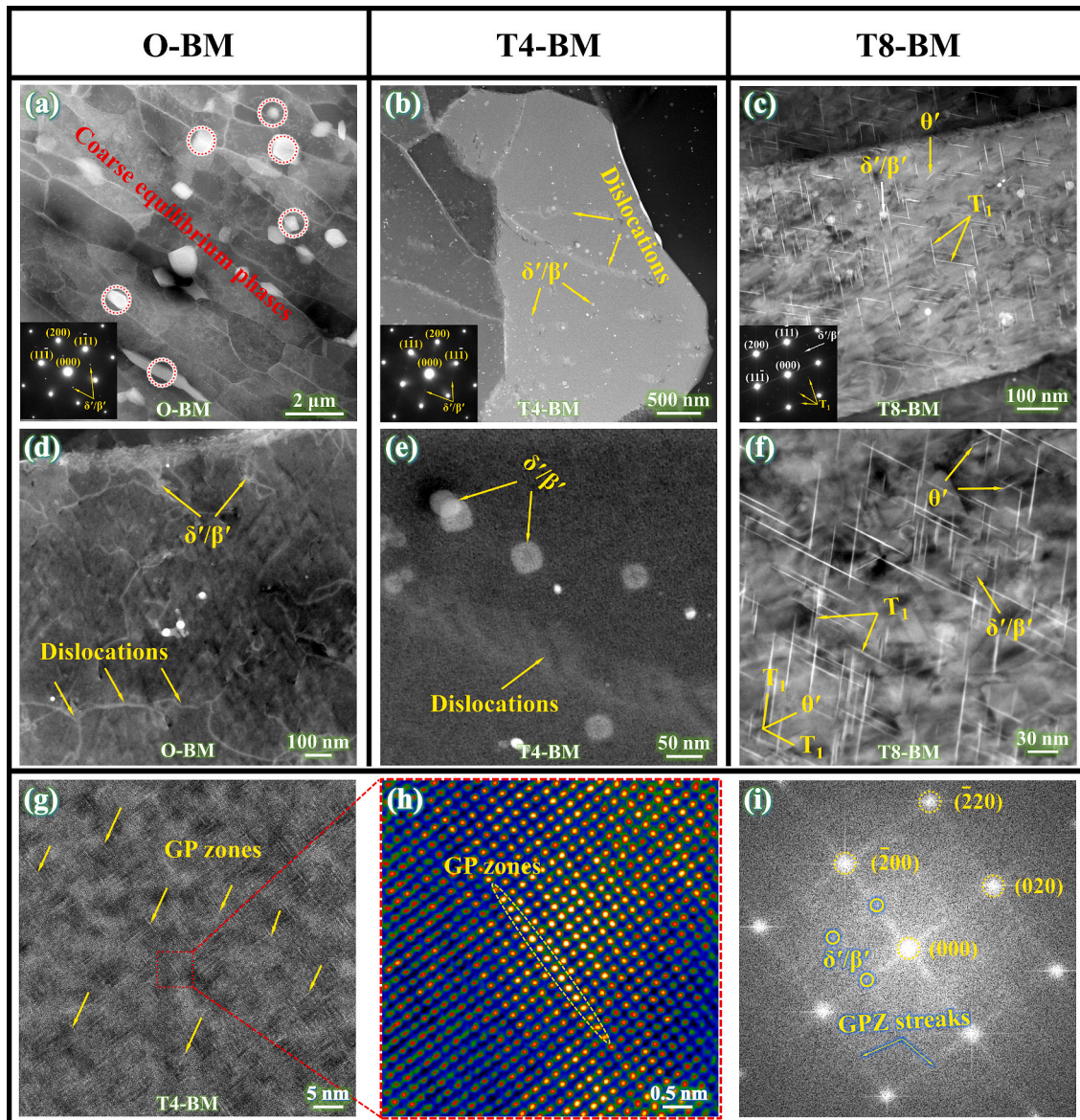
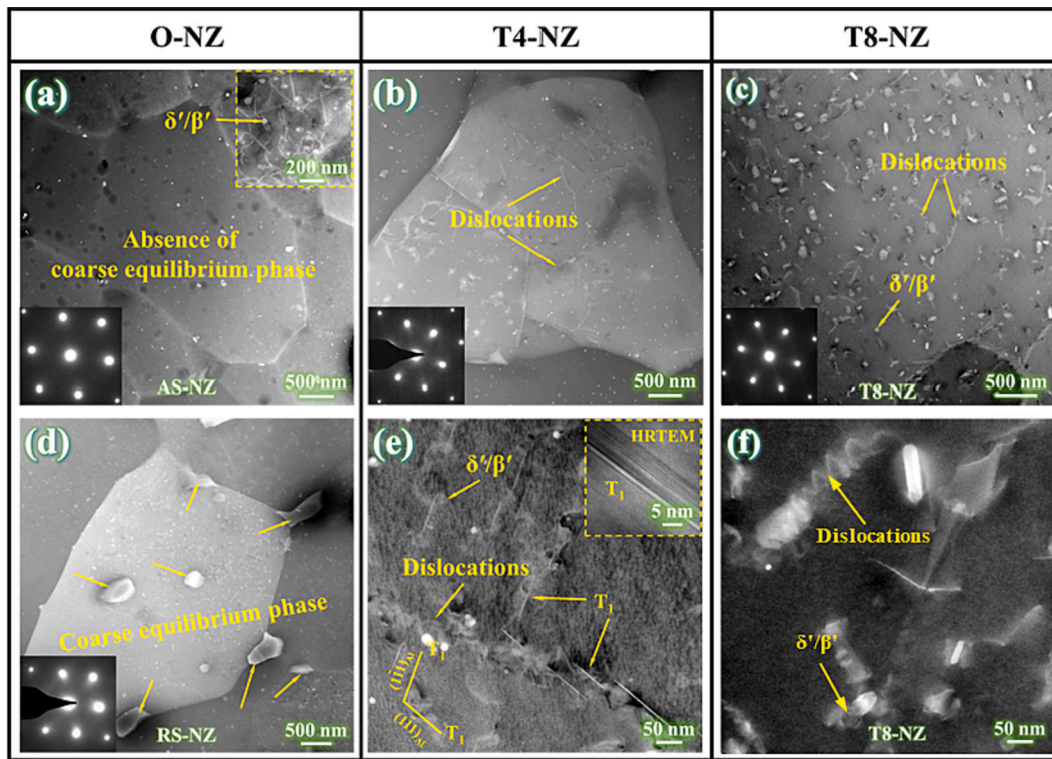
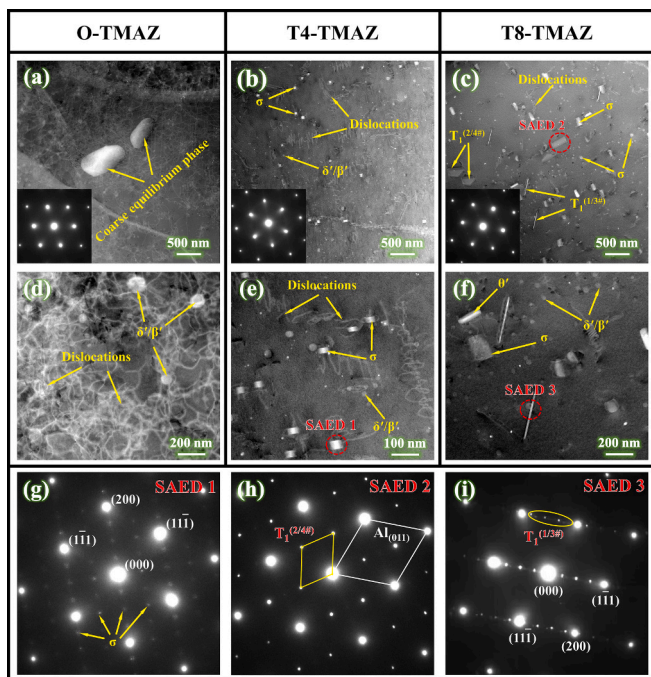


Fig. 5. Precipitates of the BM developed in different temper conditions: (a, d) STEM-BF and SAED images of O-BM along  $[011]_{Al}$ ; (b, e) STEM-BF and SAED images of T4-BM along  $[011]_{Al}$ ; (c, f) STEM-BF and SAED images of T8-BM along  $[011]_{Al}$ ; (g, h) HRTEM images of T4-BM along  $[001]_{Al}$  and (i) corresponding FFT patterns.





**Fig. 6.** Precipitates of the NZ of different joints: (a, d) STEM-BF and SAED images of the AS-NZ and RS-NZ in joints of 2195-O along  $[011]_{Al}$ ; (b, e) STEM-BF, SAED and HRTEM images of T4-NZ along  $[011]_{Al}$ ; (c, f) STEM-BF and SAED images of T8-NZ along  $[011]_{Al}$ .



**Fig. 7.** Precipitates of the TMAZ of different joints: (a, d) STEM-BF and SAED images of O-TMAZ along  $[011]_{Al}$ ; (b, e) STEM-BF and SAED images of T4-TMAZ along  $[011]_{Al}$ ; (c, f) STEM-BF and SAED images of T8-TMAZ along  $[011]_{Al}$ ; (g-i) SAED patterns corresponding to the marked positions in (e, c and f).

TMAZ), indicating the generation of many of  $\delta'/\beta'$  and dislocations. Some cubic-shape precipitates are detected and have been demonstrated to be the  $\sigma$  ( $Al_5Cu_6Mg_2$ ) according to the morphology and SAED analysis, as shown in Fig. 7e and g.

In the TMAZ of 2195-T8 joint (T8-TMAZ), most of the original  $T_1$  precipitates are dissolved, as shown in Fig. 7c and f. The residual  $T_1$  in the T8-TMAZ is dramatically coarsened (Fig. 7c and i), developing a size of 200–400 nm in length and 8–15 nm in thickness. Besides, a few elliptical-shape precipitates are detected and identified to be the  $T_1^{(2/4\#)}$  using SAED analysis (Fig. 7c and h).  $\delta'/\beta'$  (10–70 nm) and  $\theta'$  (150–200 nm in length and 20–30 nm in thickness) are coarsened, and the cubic-shape phase  $\sigma$  ( $Al_5Cu_6Li_2$ ) is also detected in this region.

### 3.2.4. Precipitates in the LHZ

The generation of the lowest hardness zone (LHZ) is one of the typical features in the FSW joints of precipitation strengthening Al alloys [34]. According to the hardness profiles of the three joints in Fig. 2, the LHZ is found obviously in 2195-T8 joints, not slightly in 2195-T4 joints and absent in 2195-O joints. Thus, precipitates of the LHZ in 2195-T4 joint (T4-LHZ) and 2195-T8 joints (T8-LHZ) are studied by TEM, as shown in Fig. 8. The LHZ is so narrow ( $< 0.5$  mm) that the TEM observation samples of this region are prepared combining micro-hardness test and FIB process, as shown in Fig. 8a and d. This implies that the location of the LHZ is determined by hardness analysis, and the sample is obtained by FIB.

According to the Fig. 8,  $T_1$ ,  $\delta'/\beta'$ ,  $\sigma$ , grain boundary phases (GBPs) and precipitate-free zone (PFZ) are clearly observed in the LHZ of the both joints. Coarse  $T_1$  precipitates with four variants, including needle-shape  $T_1^{(1/3\#)}$  and elliptical-shape  $T_1^{(2/4\#)}$ , are evidently observed in the LHZ of the two joints. The needle-shape  $T_1^{(1/3\#)}$  appears in a length of 50–500 nm and a thickness of 2–10 nm in the T4-LHZ, which is bigger (120–250 nm and a thickness of 4–8 nm) in the T8-LHZ. The elliptical-shape  $T_1^{(2/4\#)}$  has a similar size (about 160 nm) in the LHZ of the two joints. The  $\delta'/\beta'$  precipitates are coarsened with a diameter of 20–120 nm. Both of  $\sigma$  and GBPs are bigger in the T4-LHZ than in the T8-LHZ, and the PFZ is also wider in the T4-LHZ ( $480 \pm 50$  nm) than in the T8-LHZ ( $250 \pm 30$  nm). The coarsened  $\theta'$  is also detected in the T8-LHZ, as shown in Fig. 8f. In addition, some rod-shaped precipitates marked by



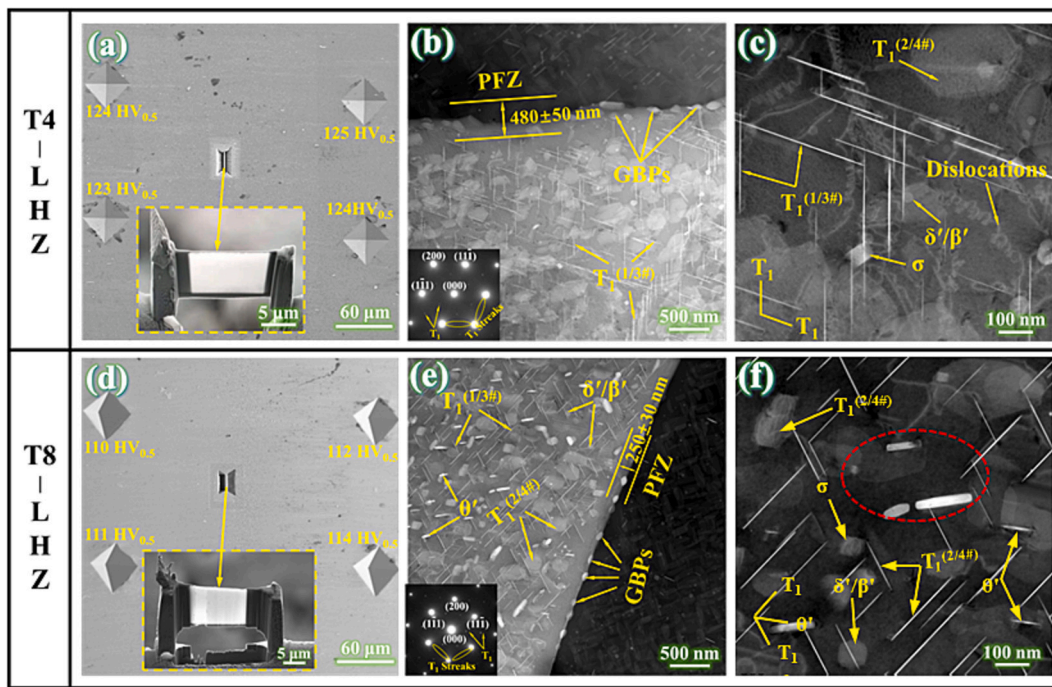


**Fig. 8.** Precipitates of the LHZ of 2195-T4 and 2195-T8 joints: (a) TEM sample preparation of the T4-LHZ by SEM-FIB; (b, c) STEM-BF and SAED images of the T4-LHZ along  $[011]_{\text{Al}}$ ; (d) TEM sample preparation of the T8-LHZ by SEM-FIB; (e, f) STEM-BF and SAED images of the T8-LHZ along  $[011]_{\text{Al}}$ .

red circles in Fig. 8f might be other equilibrium phases ( $T_2$  or  $T_B$ ) [16,28].

### 3.2.5. Precipitates in the HAZ

Precipitates of the HAZ in the three joints are exhibited in Fig. 9. According to Fig. 9a and d, a lot of coarse equilibrium phases and fine  $\delta'/\beta'$  are observed in the HAZ of 2195-O joint (O-HAZ), which is in

agreement with the precipitate observation of the O-BM (Fig. 5a and d).

In the HAZ of 2195-T4 joint (T4-HAZ), many fine needle-shape  $Ti_3Al$  (about 40–80 nm in length and 2–5 nm in thickness) are observed on dislocations and sub-grain/gain boundaries, as shown in Fig. 9b and e. As compared with the T4-BM (Fig. 2b and e), a few  $\delta'/\beta'$  are coarsened in the T4-LHZ with a diameter of 30–80 nm.

Precipitates are coarsened in the HAZ of 2195-T8 joint (T8-HAZ)

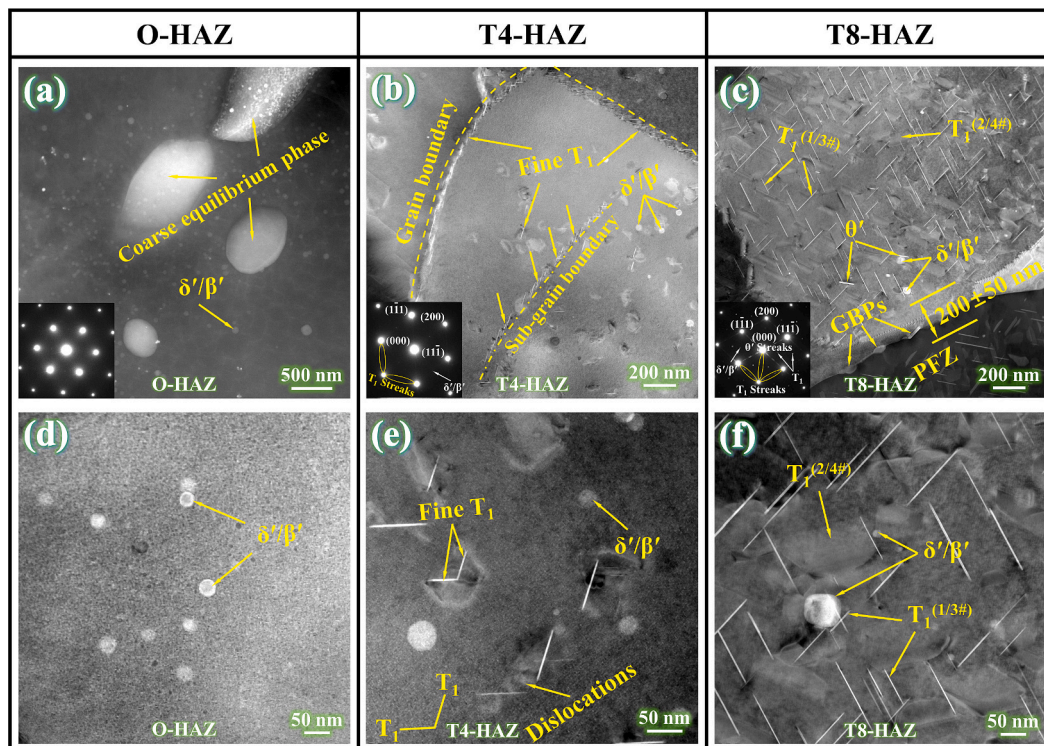


**Fig. 9.** STEM-BF and SAED images of precipitates in the HAZ of different joints along  $[011]_{Al}$ : (a, d) the O-HAZ; (b, e) T4-HAZ; (c, f) T8-HAZ.

comparing with the T8-BM, as shown in Fig. 2e and f. In the T8-HAZ, the  $T_1$  precipitates are observed with four variants, including the needle-shape  $T_1^{(1/3\#)}$  (about 40–80 nm in length and 2–5 nm in thickness) and the elliptical-shape  $T_1^{(2/4\#)}$  (about 170 nm in diameter).  $\theta'$  is grown up to 40–100 nm in length and 5–10 nm in width.  $\delta'/\beta'$  precipitates are developed with a diameter of 20–80 nm. The GBPs are also formed with a size about 70 nm, and the PFZ is generated with the width of  $200 \pm 50$  nm.

### 3.3. Tensile properties

Engineering stress-strain curves and tensile properties of the base materials in different temper conditions and corresponding FSW joints are respectively exhibited in Fig. 10. Comparative analysis of the tensile properties of the base materials and joints indicates three important things: Firstly, the O-BM has the lowest base material strength (196 MPa) and joint strength (194 MPa), but develops the highest joint coefficient (99%) with little strength loss; furthermore, the 2195-O joint gets the maximal elongation, about 15%. Secondly, the T4-BM has a medium base material strength (481 MPa) but the highest joint strength (442 MPa), which develops the intermediate joint coefficient (92%) and joint elongation (12.1%), indicating less strength reduction. Thirdly, the T8-BM, have the maximum base material strength (596 MPa) and medium joint strength (431 MPa), developing the minimum joint coefficient about 72% and the most strength decrease. Besides, elongation of T8-BM condition changes slightly after welding.

Fracture morphologies and locations of the different base materials and joints are shown in Fig. 11. Fracture locations of the 2195-O joint occurs in the HAZ/BM, while both 2195-T4 and 2195-T8 joint are broken in the LHZ, as shown in Fig. 11g. Fracture surface of the O-BM and corresponding joint is characterized with large dimples (Fig. 11a and d), showing a typical ductile fracture feature. In addition, cracked particles are always observed at the bottom of the dimples.

Fracture surface of the T4-BM is characterized with numerous dimples and tearing ridges (Fig. 11b), indicating obvious ductile fracture feature. In the fracture surface of 2195-T4 joint, many intergranular cracks and micro-voids with cracked particles are observed (Fig. 11e), indicating toughness of the 2195-T4 Al–Li alloy decreasing after welding. It is noticeable that these micro-voids are aligned along grain boundaries, which can be the sources of crack initiation leading to the early fracture of the joints [35]. Therefore, the tensile failure of the T4-BM is presented with obvious toughness fracture mechanism, while the 2195-T4 joint is broken with a dominant toughness-brittleness mixed fracture feature.

Fracture surface of the T8-BM contains many intergranular cracks

and smooth cleavage facets, while in the 2195-T8 joint a lot of tearing ridges and shallow dimples are developed, as shown in Fig. 11c and f. Besides, large micro-voids with cracked particles at the bottom are generated along grain boundaries. Thus, toughness-brittleness mixed fracture is the dominant fracture mechanism for the BM and joint.

## 4. Discussion

### 4.1. Precipitates in 2195 Al–Li alloy

2195 Al–Li alloy belongs to Al–Cu–Li alloys, which has extremely complex precipitate systems and a certain natural aging tendency [14,36].  $T_1$  is the dominant strengthening precipitate for the peak aging temper condition (T8) of 2195 Al–Li alloy, supporting high tensile strength of this alloy.  $\theta'$  is a kind of very important strengthening precipitate in Al–Cu alloys, with or without Li, which can be detected in 2195-T8 Al–Li alloy with  $T_1$  sufficiently developing.  $\delta'$  and  $\beta'$  known as metastable precipitates are both easy to nucleate at low temperature due to low activation and interfacial energy. Thus,  $\delta'/\beta'$  are always formed during the natural aging process and observed in all temper conditions of 2195 Al–Li alloy. During the FSW of 2195 Al–Li alloy,  $\delta'$  always dissolves in the matrix due to elevated temperature at first, but re-precipitates at the cooling process and even coarsens in a big size when suffers high temperature. The  $\delta'$  often arises with the  $\beta'$  which mostly experiences precipitation and coarsening during the welding [14].

2195-T4 Al–Li alloy is produced by solution and natural aging treatment, in which most of solute atoms are reserved in the matrix with the development of large solute clusters (GP zones). Therefore, this alloy is mainly enhanced by solid solution strengthening with good strength and plasticity. 2195-O Al–Li alloy has experienced sufficient annealing process, leading to the solutes precipitating into large equilibrium phases, such as  $T_B$ ,  $Al_7Cu_2Fe$ , T and  $\theta$ , which has been reported in our previous paper [27]. Thus, this alloy has the minimum strength and good elongation. Significant difference of precipitate components in different temper conditions of the BM leads to variant precipitate evolution and mechanical properties of this alloy during FSW.

### 4.2. Precipitates and hardness evolution of 2195 Al–Li alloy FSW joints

Mechanical properties of 2195 Al–Li alloy are mainly determined by the type, size, content and distribution of precipitates. The precipitation, in turn, depends on the chemistry, grain structure and hot work history of the alloy. The transient and gradient change in strain, strain rate, and temperature are inherent during the FSW process [37]. Therefore, the

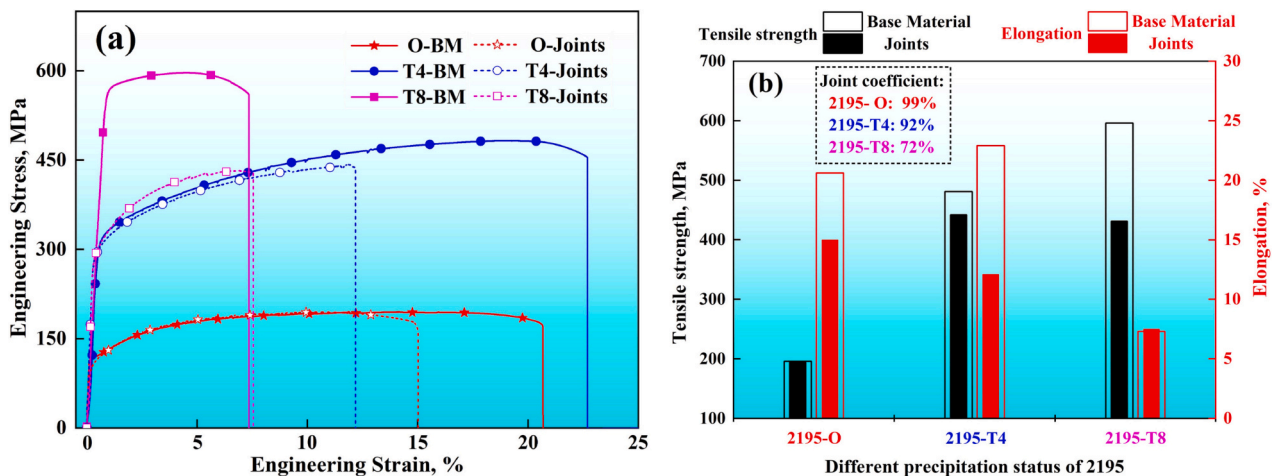


Fig. 10. Engineering stress-strain curves and tensile properties of different 2195 Al–Li alloys and their welding joints: (a) Engineering stress-strain curves; (b) tensile strength and elongation.



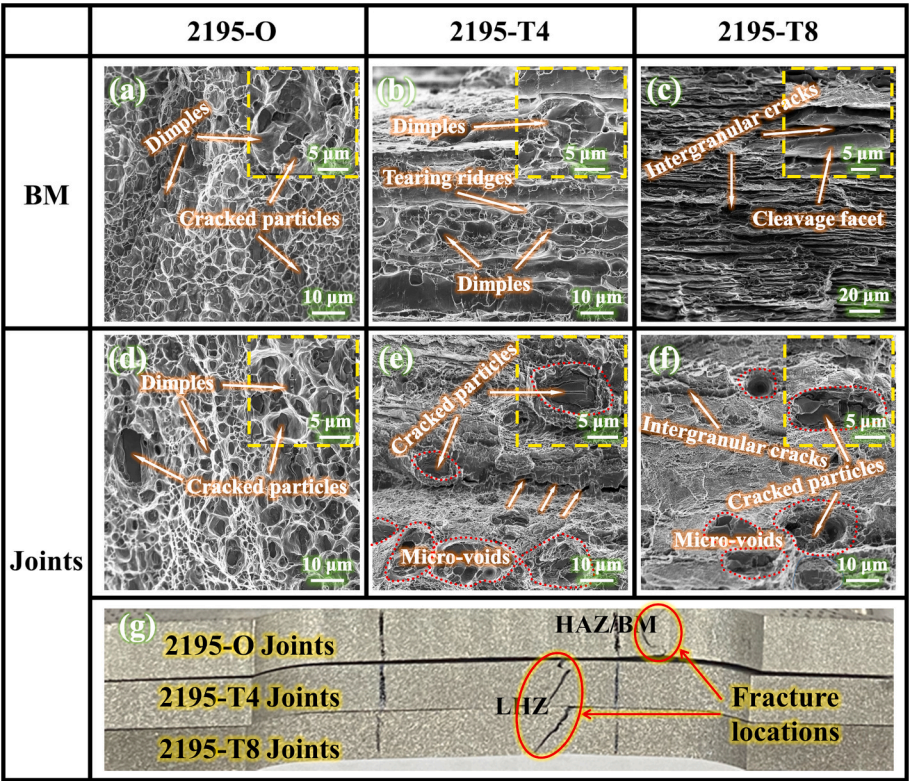


Fig. 11. SEM fractographs of (a, d) 2195-O, (b, e) 2195-T4, (c, f) 2195-T8 Al—Li alloys and corresponding FSW joints, and (g) fracture samples of the different FSW joints.

distribution, size, and types of precipitates are characterized as sharp spatial gradients in the transition from the BM to the NZ, resulting in a variant hardness distribution [38]. Based on the correlation between precipitate evolution and hardness distribution, precipitates in the typical regions, i.e., BM, HAZ, LHZ, TMAZ and NZ, of 2195 Al—Li alloy FSW joints developed in different temper conditions of base material are summarized in Fig. 12.

4.2.1. Precipitates evolution and hardness distribution in the HAZ and LHZ

The HAZ mainly experiences the FSW thermal cycle, but is not

affected by plastic deformation. Thus, as compared with the BM, same grain structure remains in this region, while precipitates are distinctly changed due to the thermal exposure. Generally, the HAZ of 2xxx Al alloy FSW joints experiences the maximum temperature of 390 °C during the FSW [23,29,34–39]. Moreover, this region is always wider than other regions in the FSW joints, having wide variation on temperature change and developing complicated precipitation behavior. The LHZ, which is transition zone located between the HAZ and TMAZ, actually belongs to the HAZ and suffers a higher welding temperature within the HAZ.

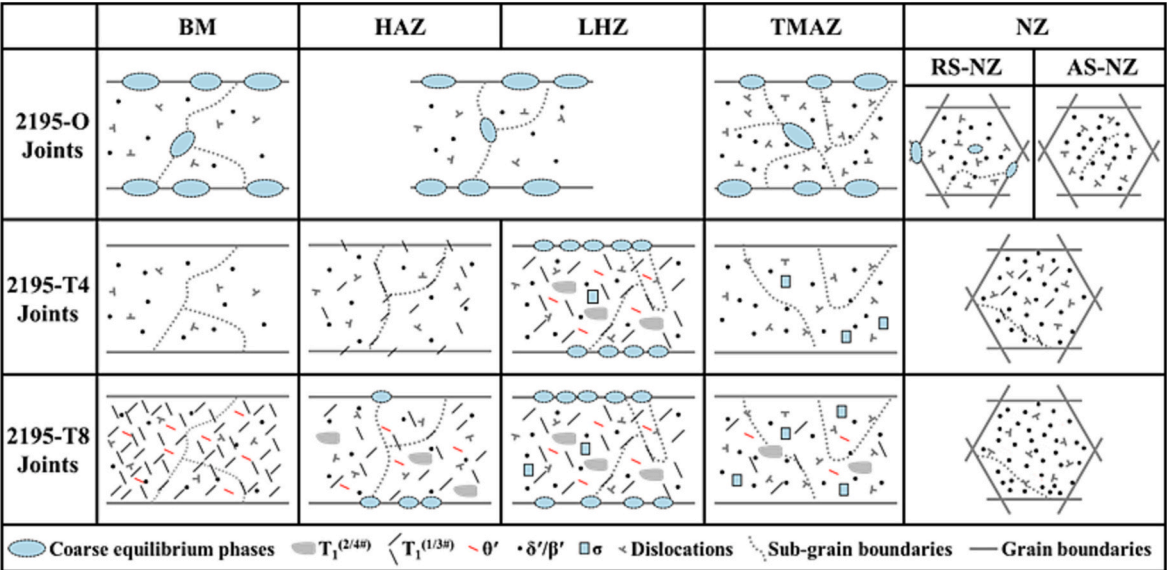


Fig. 12. Schematic diagrams of STEM-BF micrographs in  $\langle 011 \rangle_{\text{Al}}$  direction showing precipitate evolution of different 2195 Al—Li alloy FSW joints.

During FSW, the HAZ is mainly affected by welding thermal cycle which can be considered as a heat treatment process to this region. As is known to all, the general heat treatments to aluminum alloy are solution, artificial aging and annealing. Peak welding temperature of the HAZ in 2xxx Al alloy FSW joints is about 390 °C, which cannot lead to obvious solution action, as the solution temperature is >500 °C. The base material has been annealed at a high temperature ( $\geq 400$  °C) with sufficient time, leading to most solute atoms precipitating into equilibrium phases. The welding temperature of the HAZ is lower than the annealing temperature, which cannot promote more solute atoms precipitating. Therefore, artificial aging can hardly occur in the O-HAZ during FSW. Aluminum alloy annealing refers to the process of heating aluminum alloy to a specific temperature (usually ranging from 300 °C to 500 °C), holding it at that temperature for a certain amount of time, and then allowing it to cool naturally. Thus, the thermal history of the HAZ should be a short time annealing process, which mainly promotes dislocation motivation.

Subjected to high temperature heat treatment with enough duration (>24 h), 2195 Al—Li alloy displays its maximum softness when completely annealed due to reduced solid solution atomic content and numerous coarse equilibrium phases. Therefore, no obvious LHZ generated in the 2195-O joints, as the hardness can hardly decrease by the thermal cycle to solid precipitation and phase coarsening.

In the T4-BM, most of solute atoms are reserved in the matrix and easily form into precipitates when heated. Hence, the FSW heat input can be considered as a quick artificial aging to the T4-HAZ, mainly resulting in the formation of  $T_1$ . Normally,  $T_1$  is formed in nanometer size during the aging process at low temperatures, about 100 °C to 140 °C [40,41]. This precipitate can intensively coarsen into a few micrometers in length when it is comparable to the critical size for particle-stimulated nucleation (PSN) [15]. Moreover, the significant growth of  $T_1$  can occur at higher temperature, ranging from 250 °C to 310 °C [14,16]. The precipitation degree of  $T_1$  is dependent on the peak temperature and duration above the artificial aging temperature.

In the individual regions of the T4-HAZ, welding temperature decreases with the distance to the TMAZ increasing. Thus, within the HAZ, less and smaller  $T_1$  is observed in the region '4' as compared with the region '3' (Fig. 3, LHZ). It has been reported that the peak temperature of the LHZ reaches approximately 390 °C, a level intense enough to stimulate the precipitation of  $T_1$ . Therefore,  $T_1$  in large thickness is formed in the T4-LHZ, even the elliptical-shape  $T_1^{(2/4\#)}$  being observed. Despite an increased occurrence of  $T_1$  precipitates within the T4-HAZ, there has been a relatively minimal shift in hardness attributed to the bare presence of a minor quantity of these precipitates. The emergence of  $T_1$  fails to augment the hardness of LHZ, rather it diminished its hardness. This phenomenon is due to the precipitate strengthening predominantly contributed by the coarse and scarce  $T_1$  is restrained, while simultaneously the solid-solution strengthening is weakened consequent to the solute precipitation.

The high solute contents of 2195-T4 alloy can also provide large solute atoms for precipitate forming due to the high welding temperature. So, in the T4-LHZ, some Cu enrichment phases are generated at the grain boundaries (GBPs) and grain interior. Furthermore, the generation of GBPs can promote the PFZ generating due to solute depletion. Generally, the GBPs with the PFZ will act as void/crack sources, accelerating propagation of cracks along the grain boundaries and contributing to early failure.

The T8-BM has experienced peak aging process, resulting in sufficient precipitation and development of  $T_1$ . Thermal cycle during the welding can be considered as a quick over-aging at high temperature to the T8-HAZ, mostly leading to the occurrence of precipitate growing. It is worth noting that the temperature above 350 °C can cause obvious dissolution of  $T_1$  [14]. Thus, part of the original  $T_1$  can be dissolved in the matrix, and the residual is significantly coarsened, even leading to the elliptical-shape  $T_1$  being detected (Fig. 9c). The softening of the HAZ is mainly attributed to the dissolution and coarsening of  $T_1$ . The lowest

hardness generated in the T8-HAZ is resulted from the maximum degree of the dissolution and coarsening of  $T_1$ , and also the development the GBPs and PFZ. Moreover, the dissolution of  $T_1$  can supply more solute atoms to promote fine precipitates ( $\sigma$  and  $\delta'/\beta'$ ) forming in the subsequent cooling process. The thermal exposure can accelerate solutes segregating at grain boundaries, leading to the generation of GBPs and PFZs. Since the higher number density of precipitates and the less solute content, the PFZs appears narrower in the T8-LHZ than that in the T4-LHZ.

#### 4.2.2. Precipitates evolution and hardness distribution in the TMAZ

Relatively higher welding temperature and plastic deformation occur in the TMAZ than in the HAZ [38]. The thermal cycles lead to dissolution, precipitation and coarsening of precipitates [17,21]. However, in the O-TMAZ, the original equilibrium phases change a little, attributed to the high stability of these phases. The deformation leads to the development of dislocations and sub-grains in large amount generating working hardening. Jointly with the effect of the heat input, a lot of  $\delta'/\beta'$  forms in the O-TMAZ, resulting in a few increases of hardness. In addition, more dislocations are generated in the O-TMAZ than the T4-TMAZ and T8-TMAZ (Fig. 7d-f), resulting from weaker of the base material in O temper condition.

The effect of heat input on the T4-TMAZ is similar to that on the T4-HAZ, indicating an artificial aging process to this region. However, little  $T_1$  is observed in the T4-TMAZ, which is significantly different with the T4-HAZ. As a competitive precipitating relationship between  $T_1$  and  $\sigma$ , the generation of  $\sigma$  ( $Al_5Cu_6Mg_2$ ) consumes Cu atoms, leading to the  $T_1$  decreases or even disappear in the TMAZ [42]. The  $\sigma$  has a cubic structure with the lattice constants of  $a = b = 0.831$  nm and commonly has an edge length ranging from 20 to 50 nm [43]. This cubic phase also has an excellent potential for strengthening, which offset the decrease of solid solution strengthening by solute precipitation, leading to the hardness of the T4-TMAZ changing a little (Fig. 2). Precipitate evolution of the T8-TMAZ is similar to the T8-HAZ, indicating that the significant dissolution and coarsening of  $T_1$  leads to decrease of hardness.

#### 4.2.3. Precipitates evolution and hardness distribution in the NZ

It has been reported that the NZ suffers the maximum plastic deformation (true strains >10) and welding temperature (400–550 °C), leading to most of precipitates dissolving in the matrix [38]. This implies that the FSW stage can be considered as a rapid solid solution to the NZ, and the cooling process after FSW should be a natural aging (T4 treatment). Precipitates dissolve in the matrix promoting the development of high density of GPZs, indicating that the NZ is strengthened by solid solution strengthening. Thus, precipitation status of the NZ is very similar to the T4-BM, leading to hardness of the T4-NZ being close to the T4-BM. Although some fine  $T_1$  has nucleated in the T4-NZ due to thermal exposure, little change of hardness is detected resulting from the low content of  $T_1$ .

In the T8-NZ,  $T_1$  and  $\theta'$  almost completely disappear leading to distinct increase of solute concentration and promoting some fine precipitates generating after welding. The effect of solid solution strengthening in the T8-NZ cannot compensate the loss of precipitation strengthening, resulting in the dramatic decrease of hardness. Hence, hardness of the T8-NZ is lower than the T8-BM.

In the O-NZ, some original equilibrium phases are still observed due to high thermal stabilization of these phases. The results are commonly found in the retreating side of the O-NZ (RS-NZ), but little in the advancing side of the O-NZ (AS-NZ), as shown in Fig. 5a and d. The main reason is that relatively higher thermal exposure, plastic deformation and material mixing are generated in the AS-NZ, which accelerate diffusion rates and shorten diffusion distances of solute atoms. Therefore, some equilibrium phases are remained in the RS-NZ, which weakens the effect of solid solution strengthening, leading to the hardness increment decreasing from AS-NZ to RS-NZ (Fig. 2).



#### 4.3. Tensile properties and fracture behavior of 2195 Al–Li FSW joints

Tensile properties of the different Al–Li alloy FSW joints are summarized in Fig. 13. It reveals that most studies are focused on artificial aged (T6 and T8) Al–Li alloys which always have high joint strength and develop a joint coefficient of 70–80% [44–46]. The softening is predominantly attributed to the reduction of precipitation strengthening due to dissolution and coarsening of strengthening precipitates [23,29]. The UTS of 2195-T8 Al–Li alloy FSW joint is lower in this study than that in some literatures, mainly owing to higher heat input under the lower welding speeds in this study [11,31].

Generally, the Al–Li alloys in natural aged (T3 and T4) temper conditions always develop a joint coefficient >85% [47–49]. The strength loss is mainly resulted from the decrease of solid solution strengthening due to solute concentration reducing. The ductility reduction is related to the heterogeneous distribution of microstructure (grain morphologies, size and orientation, and precipitate distribution) [48,49]. Generally, joint strength of the natural aged Al alloys is lower than the artificial aged Al alloys, and joint strength the former can be significantly improved by a simple post weld heat treatment. However, as a final state material, the artificial aged Al alloys are not suitable for more heat treatment. Therefore, higher tensile strength is potential to obtain in the 2195-T4 joint as compared with the 2195-T8 joint. Malard et al. reported that the 2050-T34 Al–Li FSW joint is significantly enhanced by the heat treatment of 30 h at 150 °C [25]. Hakan et al. found the T6 treatment after welding can raise tensile strength of 2024-T4 Al alloy FSW joint about 10.5% [50].

Friction stir welding of the Al–Li alloy in O condition is seldom reported in public. In this study, joint strength is dramatically lower in the O state alloy than in the other two alloys, but the maximum joint coefficient is obtained in the 2195-O joint. In addition, the 2195-O joint also has good ductility developing the highest joint elongation, about 15%.

Both of 2195-T8 joint and 2195-T4 joint are fractured at the LHZ, which is in accord with the fracture feature of most precipitation-hardened aluminum alloy FSW joints [38]. The HAZ and BM are the weaker regions in the 2195-O joint, indicating that fracture behavior of the joint also follows the other two joints in this study. Microstructure features of the broken joints close to the fracture surface are analyzed by

STEM observation, as shown in Fig. 14. Numerous cracked GBPs along grain boundaries are found in the three joints (Fig. 14a–c). Moreover, dislocations are tangled around the uncracked GBPs, and some tangled dislocations and dislocation walls are clearly observed in the grains adjacent to this phase. Thus, fracture process of these joints can be revealed in Fig. 15: (i) dislocations randomly distribute within grains at first, and then start to move with the tensile stress accumulating, leading to the occurrence of localized slip; (ii) the combination of GBPs and PFZ allows localized slip to generate stress concentrations near the GBPs and PFZ, promoting cracks and micro-voids nucleating at the GBPs; in addition, complicated dislocation motions result in tangled dislocations and dislocation walls developing at grain inners (iii) the cracks and micro-voids grow up with stress concentration exacerbating; (iv) the adjacent cracks merge together during the growing up, and extend along grain boundaries, leading to the joint fracture, finally; the micro-voids coalesce and develop in big size with the cracked GBPs being generated at the bottom. Thus, fracture of the three joints is related to the generation of GBPs and PFZ, in this study.

#### 5. Conclusion

In this paper, three temper conditions (O, T4 and T8) of 2195 Al–Li alloy plates are subjected to friction stir welding (FSW), and precipitates and mechanical properties of the three FSW joints are discussed in detail. The main conclusions can be drawn as follows:

- (1) In the 2195-O FSW joint, the original equilibrium phases, including  $\theta$ ,  $T_B$ ,  $T$  and  $Al_7Cu_2Fe$ , are almost completely dissolved in the AS-NZ, but are partially dissolved in the RS-NZ in which the phase evidently decrease in content and size. The NZ is hardened resulting from the dissolution of equilibrium phases, and the hardness increment of the NZ reduces from the AS-NZ to RS-NZ. Precipitates in the TMAZ and HAZ change a little, and the hardness of the TMAZ is increased due to the effect of work hardening and the generation of  $\delta'/\beta'$ .
- (2) In the 2195-T4 FSW joint, precipitates in the NZ and TMAZ are accord closely with the BM, excepting the nucleation a small number of  $T_1$  in the NZ and  $\sigma$  in the TMAZ. The FSW thermal

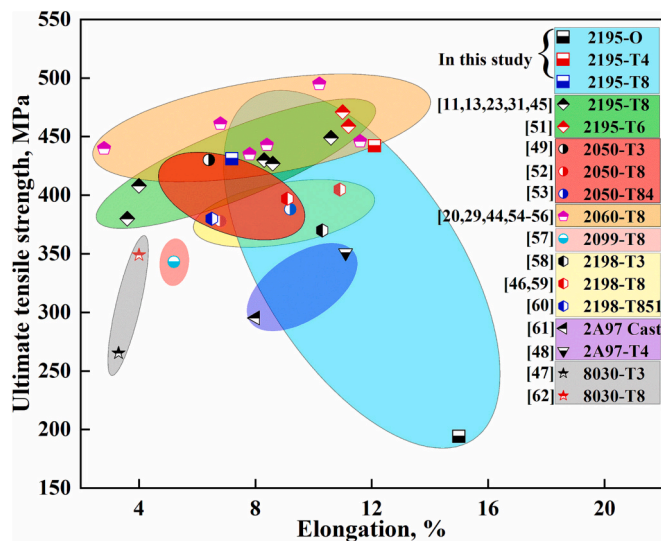


Fig. 13. The ultimate tensile strength and elongation of different Al–Li alloys [11,13,20,23,29,31,44–49,51–62]. The colour ellipses depict tensile strength and elongation of various Al–Li alloy FSW joints, for example the light blue representing 2195 Al–Li alloy FSW joints in three precipitation states within this research. (For interpretation of the references to colour in this figure legend, the reader is referred to the web version of this article.)

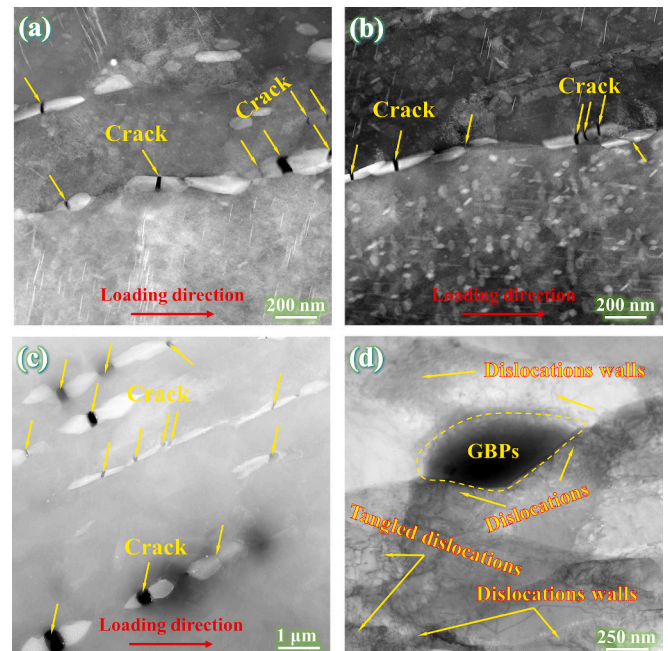


Fig. 14. STEM images about the microstructure of 2195 Al–Li FSW joints close to the fracture surface: (a) 2195-T8 joint; (b) 2195-T4 joint; (c, d) 2195-O joint.

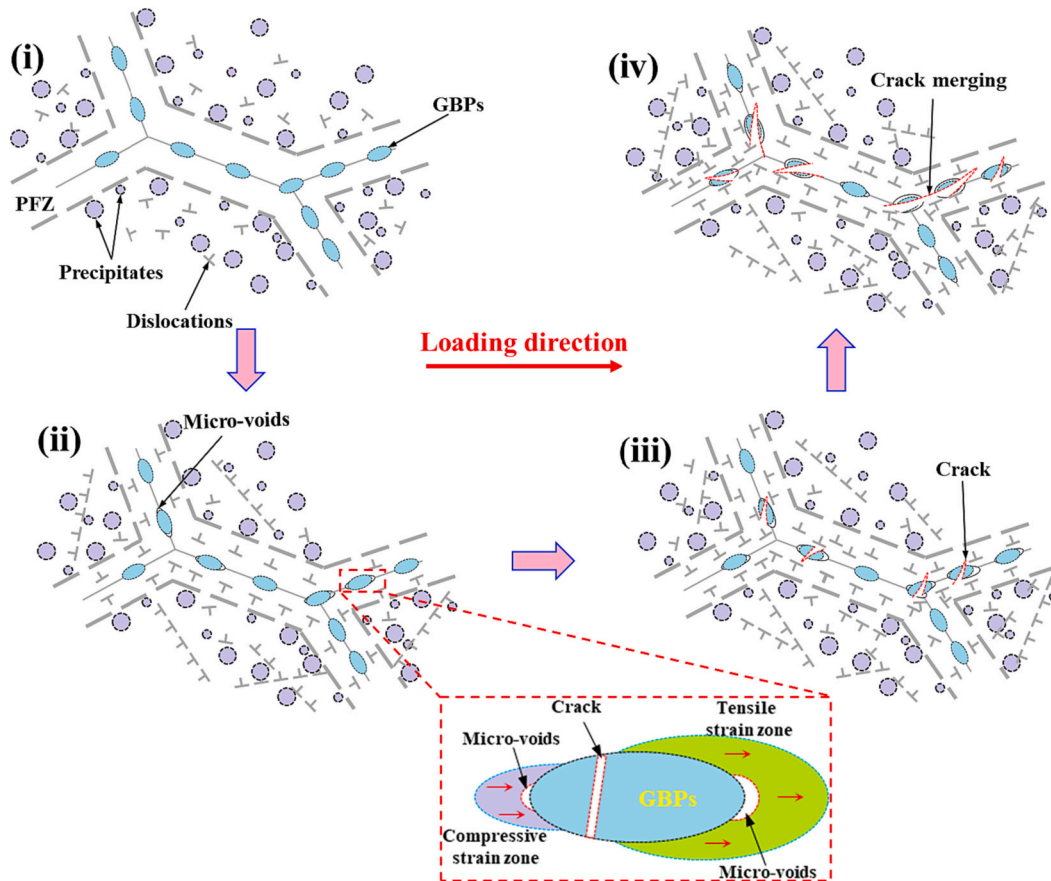


Fig. 15. The schematic of fracture process of 2195 Al–Li alloy FSW joints.

history makes an quick artificial aging to the HAZ mainly resulting in  $T_1$  forming, while only a few changes of hardness occur in this region attributed to the low precipitation degree. In the HAZ, the content and size of  $T_1$  are raised with the distance decrease to the TMAZ due to elevated heat input; the maximum precipitation of  $T_1$  is detected in the LHZ where the lowest hardness is obtained due to the generation of coarse  $T_1$ , GBPs and PFZ.

- (3) In the 2195-T8 FSW joint, the original precipitates ( $T_1$ ,  $\theta'$ ) almost completely dissolve in the NZ with a few fine particles ( $\delta'/\beta'$ ) generating; most of  $T_1$  and  $\theta'$  disappear in the TMAZ with a few  $\sigma$  developing, and the residues of the two precipitates are significantly coarsened; the welding cycles have a quick over-aging to the HAZ, in which the dissolution and coarsening of  $T_1$  and generation of GBPs and PFZ mainly result in hardness decreasing.
- (4) Hardness profile is respectively represented as a “n” shape in 2195-O joint due to significantly harden of the NZ, a “wave line” shape in 2195-T4 joint attributed to the slight change of precipitation degree, and a “w” shape in 2195-T8 joint mainly owing to the dissolution and coarsening of  $T_1$ . The three joints are all broken in their weak regions during the tensile test, and have similar fracture behavior, indicating that the crack initiation and development are related to the GBPs, PFZ and grain boundaries.

#### CRediT authorship contribution statement

**Peng Chen:** Writing – review & editing, Writing – original draft, Project administration, Funding acquisition, Data curation. **Wenhao Chen:** Investigation, Data curation. **Jiixin Chen:** Writing – review & editing, Formal analysis. **Zhiyu Chen:** Validation, Data curation. **Ruixiang Yin:** Writing – review & editing. **Yang Tang:** Investigation,

Formal analysis. **Ge Liu:** Methodology. **Bensheng Huang:** Resources, Project administration. **Zhiqing Zhang:** Supervision, Resources, Project administration.

#### Declaration of competing interest

None.

#### Data availability

Data will be made available on request.

#### Acknowledgements

This research is financially supported by Natural Science Foundation in Sichuan Province (2023NSFSC0915), Postdoctoral Research Project Special Fund in Sichuan Province, Natural Science Starting Project of SWPU (2023QHZ017) and Open Experimental Fund of SWPU (2022KSZ05020).

#### References

- [1] R.J.H. Wanhill, G.H. Bray, *Aerostructural Design and its Application to Aluminum-lithium Alloys*, Aluminum-Lithium Alloys, Elsevier, USA, 2014, pp. 27–58.
- [2] Y. Yang, J. Bi, H. Liu, et al., Research progress on the microstructure and mechanical properties of friction stir welded Al Li alloy joints, *J. Manuf. Process.* 82 (2022) 230–244.
- [3] R.J.H. Wanhill, G.H. Bray, *Aerospace Applications of Aluminum-lithium Alloys*, Aluminum-Lithium Alloys, Elsevier, USA, 2014, pp. 503–535.
- [4] T. Jiang, T. Jiao, G. Dai, et al., Microstructure evolution and mechanical properties of 2060 Al-Li alloy via friction stir additive manufacturing, *J. Alloys Compd.* 935 (2023) 168019.
- [5] R. Mishra, H. Sidhar, *Friction Stir Welding of 2xxx Aluminum Alloys Including Al-Li Alloys*, 1st ed, Elsevier, USA, 2016.



- [6] Y. Hovanski, J.E. Carsley, K.D. Clarke, et al., Friction-stir welding and processing, *JOM* 67 (2015) 996–997.
- [7] M.N. Avettand-Fènoël, R. Taillard, J. Laye, et al., Experimental investigation of three-dimensional (3-D) material flow pattern in thick dissimilar 2050 friction-stir welds, *Metall. Mater. Trans. A* 45 (2013) 563–578.
- [8] F.F. Wang, W.Y. Li, J. Shen, et al., Improving weld formability by a novel dual-rotation bobbin tool friction stir welding, *J. Mater. Sci. Technol.* 34 (2018) 135–139.
- [9] C. Gu, X. Yang, W. Tang, et al., Softening behavior of stationary shoulder friction stir welded joint for thick-plate Al-Li-Cu alloy, *J. Mater. Res. Technol.* 20 (2022) 3008–3024.
- [10] G. Zhang, C. Wu, J. Gao, Ultrasonic line source and its coupling with the tool induced heat generation and material flow in friction stir welding, *J. Mater. Res. Technol.* 21 (2022) 502–518.
- [11] H.S. Lee, J.H. Yoon, J.T. Yoo, et al., Friction stir welding process of aluminum-lithium alloy 2195, *Process. Eng.* 149 (2016) 62–66.
- [12] M.M. Attallah, H.G. Salem, Friction stir welding parameters: a tool for controlling abnormal grain growth during subsequent heat treatment, *Mater. Sci. Eng. A* 391 (2005) 51–59.
- [13] J. Zhang, X.S. Feng, J.S. Gao, et al., Effects of welding parameters and post-heat treatment on mechanical properties of friction stir welded AA2195-T8 Al-Li alloy, *J. Mater. Sci. Technol.* 34 (2018) 219–227.
- [14] J.H. Kim, J.H. Jeun, H.J. Chun, et al., Effect of precipitates on mechanical properties of AA2195, *J. Alloys Compd.* 669 (2016) 187–198.
- [15] X.Y. Wang, J.T. Jiang, G.A. Li, et al., Effects of coarse Al<sub>2</sub>CuLi phase on the hot deformation behavior of Al-Li alloy, *J. Alloys Compd.* 815 (2020) 152469.
- [16] J.A. Schneider, A.C. Nunes, P.S. Chen, et al., TEM study of the FSW nugget in AA2195-T81, *J. Mater. Sci.* 40 (2005) 4341–4345.
- [17] A.K. Shukla, W.A. Baeslack, Study of process/structure/property relationships in friction stir welded thin sheet Al-Cu-Li alloy, *Sci. Technol. Weld. Join.* 14 (2013) 376–387.
- [18] P. Chen, S.Q. Zou, J. Chen, et al., Effect of rotation speed on microstructure evolution and mechanical properties of nugget zone in 2195-T8 Al-Li alloy friction stir welding joints, *Mater. Charact.* 176 (2021) 111079.
- [19] T.F. Chung, Y.L. Yang, C.N. Hsiao, et al., Morphological evolution of GP zones and nanometer-sized precipitates in the AA2050 aluminium alloy, *Inter. J. Lightw. Mater. Manuf.* 1 (2018) 142–156.
- [20] B. Cai, Z.Q. Zheng, D.Q. He, et al., Friction stir weld of 2060 Al-Cu-Li alloy: microstructure and mechanical properties, *J. Alloys Compd.* 649 (2015) 19–27.
- [21] H. Sidhar, R.S. Mishra, Aging kinetics of friction stir welded Al-Cu-Li-mg-ag and Al-Cu-Li-mg alloys, *Mater. Des.* 110 (2016) 60–71.
- [22] Z. Shen, S. Chen, L. Cui, et al., Local microstructure evolution and mechanical performance of friction stir additive manufactured 2195 Al-Li alloy, *Mater. Charact.* 186 (2022) 111808.
- [23] P. Chen, J. Chen, S.Y. Qin, et al., Friction stir welding joints of 2195-T8 Al-Li alloys: correlation of temperature evolution, microstructure and mechanical properties, *Mater. Sci. Eng. A* 823 (2021) 141501.
- [24] H. Qin, H. Zhang, H. Wu, The evolution of precipitation and microstructure in friction stir welded 2195-T8 Al-Li alloy, *Mater. Sci. Eng. A* 626 (2015) 322–329.
- [25] B. Malard, F. De Geuser, A. Deschamps, Microstructure distribution in an AA2050 T34 friction stir weld and its evolution during post-welding heat treatment, *Acta Mater.* 101 (2015) 90–100.
- [26] A.K. Shukla, W.A. Baeslack, Study of microstructural evolution in friction-stir welded thin-sheet Al-Cu-Li alloy using transmission-electron microscopy, *Scr. Mater.* 56 (2007) 513–516.
- [27] P. Chen, T.N. Li, X. Yin, et al., The precipitate evolution in friction stir welding of 2195-O Al-Li alloy, *J. Mater. Res. Technol.* 24 (2023) 1991–2006.
- [28] R.W. Fonda, J.F. Bingert, Precipitation and grain refinement in a 2195 Al friction stir weld, *Metall. Mater. Trans. A* 37 (2006) 3593–3604.
- [29] Y. Tao, Z. Zhang, B.H. Yu, et al., Friction stir welding of 2060-T8 Al Li alloy. Part I: microstructure evolution mechanism and mechanical properties, *Mater. Charact.* 168 (2020) 110524.
- [30] C. Gao, Z. Zhu, J. Han, et al., Correlation of microstructure and mechanical properties in friction stir welded 2198-T8 Al-Li alloy, *Mater. Sci. Eng. A* 639 (2015) 489–499.
- [31] J.F. Li, Y.L. Chen, X.H. Zhang, et al., Structure and mechanical property of friction-stir weld joint of 2195-T8 Al-Li alloy plate, *Rare Metal Mater. Eng.* 47 (2018) 780–787.
- [32] M.X. Milagre, N.V. Mogili, U. Donatus, et al., On the microstructure characterization of the AA2098-T351 alloy welded by FSW, *Mater. Charact.* 140 (2018) 233–246.
- [33] W.A. Tayon, M.S. Domack, E.K. Hoffman, et al., Texture evolution within the thermomechanically affected zone of an Al-Li alloy 2195 friction stir weld, *Metall. Mater. Trans. A* 44 (2013) 4906–4913.
- [34] Z. Zhang, B.L. Xiao, Z.Y. Ma, Hardness recovery mechanism in the heat-affected zone during long-term natural aging and its influence on the mechanical properties and fracture behavior of friction stir welded 2024Al-T351 joints, *Acta Mater.* 73 (2014) 227–239.
- [35] Y.G. Hao, W. Liu, Analysis on exceptional cryogenic mechanical properties of AA2219 alloy FSW joints in multi-scale, *Mater. Sci. Eng. A* 850 (2022) 143489.
- [36] K.S. Prasad, N.E. Prasad, A.A. Gokhale, Microstructure and Precipitate Characteristics of Aluminum-lithium Alloys, *Aluminum-Lithium Alloys*, Elsevier, USA, 2014, pp. 99–137.
- [37] R.S. Mishra, Z.Y. Ma, Friction stir welding and processing, *Mater. Sci. Eng. R* 50 (2005) 1–78.
- [38] Z.Y. Ma, A.H. Feng, D.L. Chen, et al., Recent advances in friction stir welding/processing of aluminum alloys: microstructural evolution and mechanical properties, *Crit. Rev. Solid. State.* 43 (2017) 269–333.
- [39] J. Kang, Z. Feng, G.S. Frankel, et al., Friction stir welding of Al alloy 2219-T8: part I-evolution of precipitates and formation of abnormal Al<sub>2</sub>Cu agglomerates, *Metall. Mater. Trans. A* 47 (2016) 4553–4565.
- [40] R. Goswami, N. Bernstein, Effect of interfaces of grain boundary Al<sub>2</sub>CuLi plates on fracture behavior of Al-3Cu-2Li, *Acta Mater.* 87 (2015) 399–410.
- [41] X.M. Wang, G.A. Li, J.T. Jiang, et al., Influence of Mg content on ageing precipitation behavior of Al-Cu-Li-x alloys, *Mater. Sci. Eng. A* 742 (2019) 138–149.
- [42] Q. Pu, Z. Jia, Y. Kong, et al., Microstructure and mechanical properties of 2195 alloys prepared by traditional casting and spray forming, *Mater. Sci. Eng. A* 784 (2020) 139337.
- [43] B. Jiang, F. Cao, H. Wang, et al., Effect of aging time on the microstructure evolution and mechanical property in an Al-Cu-Li alloy sheet, *Mater. Sci. Eng. A* 740 (2019) 157–164.
- [44] L. Ma, S. Niu, S. Ji, et al., Comparative study of 2060-T8 Al-Li alloy friction stir welded joints between natural cooling and water cooling, *Arch. Metall. Mater.* 65 (2020) 305–312.
- [45] Q.S. Zhang, A. Yan, K. Chen, et al., Effect of tool traverse speed on joint line remnant and mechanical properties of friction stir welded 2195-T8 Al-Li alloy joints, *High Temp. Mat. Pr-isr.* 42 (2023) 20220265.
- [46] Y. Tao, D.R. Ni, B.L. Xiao, et al., Origin of unusual fracture in stirred zone for friction stir welded 2198-T8 Al-Li alloy joints, *Mater. Sci. Eng. A* 693 (2017) 1–13.
- [47] A.S. Khan, V.J. Badheka, A.B. Chaudhari, et al., Experimental investigation of friction stir welding of aluminum alloy AA8090-T3 using taguchi method, *J. Mater. Eng. Perform.* 32 (2023) 4787–4795.
- [48] H. Chen, L. Fu, P. Liang, Microstructure, texture and mechanical properties of friction stir welded butt joints of 2A97 Al Li alloy ultra-thin sheets, *J. Alloys Compd.* 692 (2017) 155–169.
- [49] M. Dhondt, I. Aubert, N. Saintier, et al., Mechanical behavior of periodical microstructure induced by friction stir welding on Al-Cu-Li 2050 alloy, *Mater. Sci. Eng. A* 644 (2015) 69–75.
- [50] H. Aydın, A. Bayram, A. Uğuz, et al., Tensile properties of friction stir welded joints of 2024 Aluminum alloys in different heat-treated-state, *Mater. Des.* 30 (2009) 2211–2221.
- [51] L. Shi, X. Dai, C. Tian, et al., Effect of splat cooling on microstructures and mechanical properties of friction stir welded 2195 Al-Li alloy, *Mater. Sci. Eng. A* 858 (2022) 144169.
- [52] B. Anandan, M. Manikandan, Machine learning approach with various regression models for predicting the ultimate tensile strength of the friction stir welded AA 2050-T8 joints by the K-fold cross-validation method, *Mater. Today Commun.* 34 (2023) 105286.
- [53] S. Kumar, D. Sethi, S. Choudhury, et al., An experimental investigation to the influence of traverse speed on microstructure and mechanical properties of friction stir welded AA2050-T84 Al-Cu-Li alloy plates, *Mater. Today: Pro.* 26 (2020) 2062–2068.
- [54] Y.Q. Mao, L.M. Ke, F.C. Liu, et al., Effect of welding parameters on microstructure and mechanical properties of friction stir welded joints of 2060 aluminum lithium alloy, *Int. J. Adv. Manuf. Technol.* 81 (2015) 1419–1431.
- [55] H. Liu, Y. Hu, C. Dou, et al., An effect of the rotation speed on microstructure and mechanical properties of the friction stir welded 2060-T8 Al-Li alloy, *Mater. Charact.* 123 (2017) 9–19.
- [56] K. Yan, T.Y. Wang, H. Liang, et al., Effects of rotation speed on microstructure and mechanical properties of 2060 Al-Cu-Li alloy in friction stir welding, *J. Mater. Eng. Perform.* 27 (2018) 5803–5814.
- [57] A.R. Cisko, J.B. Jordon, R.L. Amaro, et al., A parametric investigation on friction stir welding of Al-Li 2099, *Mater. Manuf. Process.* 35 (2020) 1069–1076.
- [58] C. Bitondo, U. Prisco, A. Squilace, et al., Friction-stir welding of AA 2198 butt joints: mechanical characterization of the process and of the welds through DOE analysis, *Int. J. Adv. Manuf. Technol.* 53 (2011) 505–516.
- [59] Y. Tao, Z. Zhang, P. Xue, et al., Effect of post weld artificial aging and water cooling on microstructure and mechanical properties of friction stir welded 2198-T8 Al-Li joints, *J. Mater. Sci. Technol.* 123 (2022) 92–112.
- [60] T.L. Jolu, T.F. Morgeneyer, A. Denquin, et al., Microstructural characterization of internal welding defects and their effect on the tensile behavior of fsw joints of AA2198 Al-Cu-Li alloy, *Metall. Mater. Trans. A* 45 (2014) 5531–5544.
- [61] G.D. Sun, L. Zhou, Y.N. Liu, et al., Microstructure characterization and evaluation of mechanical properties in 2A97 aluminum-lithium alloys welded by stationary shoulder friction stir welding, *J. Mater. Res. Technol.* 16 (2022) 416–432.
- [62] E. Lertora, C. Gambaro, AA8090 Al-Li alloy FSW parameters to minimize defects and increase fatigue life, *Int. J. Mater. Form.* 3 (2010) 1003–1006.